https://doi.org/10.1016/j.ijimpeng.2017.10.004

Characterizing Hypervelocity (> 2.5 km/s)-impact-engendered Damage in Shielding Structures Using *in-situ* Acoustic Emission: *Simulation and Experiment*

Menglong LIU[a#], Qiang WANG[b], Qingming ZHANG[c], Renrong LONG[c] and Zhongqing SU[a*]

[a]Department of Mechanical Engineering,
The Hong Kong Polytechnic University, Kowloon, Hong Kong SAR

[b]School of Automation, Nanjing University of Posts and Telecommunications
Nanjing, Jiangsu, 210023, P.R. China

[c]State Key Laboratory of Explosion Science and Technology,
Beijing Institute of Technology, Haidian District, Beijing, 100081, P.R. China

Submitted to *International Journal of Impact Engineering*

(initially submitted on 3rd January 2017; revised and re-submitted on 25th August 2017; further revised and re-submitted on 4th October 2017)

[#] PhD student; currently a Research Scientist at the Institute of High Performance Computing under the Agency for Science, Technology and Research of Singapore
∗ Corresponding author. Tel.: +852-2766-7818; fax: +852-2365-4703. Email: Zhongqing.Su@polyu.edu.hk (Prof. Zhongqing Su, *Ph.D.*)

Abstract

Pervasive in outer space, hypervelocity impact (HVI), caused by man-made debris (a.k.a. space junk) and natural micrometeoroids, poses a clear and tremendous threat to the safe operation of orbiting spacecraft, and it will possibly lead to the failure of a space exploration mission. Addressing such an issue, damage in a downscaled two-layer space shielding assembly, engendered by HVI events with an impact velocity up to 4 km/s, was characterized quantitatively, using *in-situ* measured acoustic emission (AE) induced under HVI. A hybrid model, based on three-dimensional smooth-particle hydrodynamics and finite element, was developed, to achieve insight into the traits of HVI-induced AE waves and HVI-caused damage. Proof-of-concept simulation was accomplished using the hybrid model, in which a projectile, at various impact velocities, impinged a series of shielding assembly of different thicknesses, in a normal or oblique manner. Experimental validation was implemented, and HVI-induced AE waves were *in-situ* acquired with a built-in piezoelectric sensor network integrated with the shielding assembly. Results from simulation and experiment show qualitative consistency, demonstrating the capability of the hybrid model for depicting HVI-produced shock waves, and the feasibility of *in-situ* measurement of HVI-induced AE signals. Taking into account the difference and uniqueness of HVI against other ordinary impact cases, an enhanced, *delay-and-sum*-based imaging algorithm was developed in conjunction with the built-in sensor network, able to "visualize" HVI spots in pixelated images accurately and instantaneously.

Keywords: hypervelocity impact; acoustic emission; space structures; impact detection; damage detection

1. Introduction

The recent quantum leap in space technology has intensified innovative quests by humans to penetrate outer space. A great number of spacecraft can now be found in low Earth and geosynchronous orbits, circling Earth with a velocity of the order of kilometers per second. However, the cluttering of meteoroids and man-made orbital debris (MOD, colloquially called *space junk*), which are ubiquitous in the Earth orbit, may pose an impending threat to the safety and integrity of orbiting spacecraft. MOD particles, though small in size, travel at such high speeds that even a small object can puncture the shielding layer of spacecraft and then impinge inner structures. This sort of impact is commonly referred to as "hypervelocity impact" (HVI) – a scenario in which the impact velocity (> 1 km/s usually) is at such a high degree that the strength of the materials upon impact is sufficiently small compared to their inertial forces [1, 2]. Day by day, massive space junk from abandoned, exploded and collided space vehicles emerges, and becomes new MOD. According to NASA, 20,000+ pieces of MOD particles larger than 10 cm, 500,000+ sized between 1 and 10 cm, and tens of millions smaller than 1 cm, are conservatively estimated to exist in low Earth and geosynchronous orbits [3]. The impact from any of them to spacecraft can functionally compromise the craft's integrity, possibly resulting in immediate mission abortion with catastrophic consequences. Representatively, in 1996, MOD particles from a French rocket, which had exploded a decade earlier, impacted a French satellite, leading to vast damage to the satellite [4]. In 2007, a de-commissioned meteorological satellite was destroyed by a missile in an anti-satellite test. Although this HVI event was intentionally introduced by China for removing the de-commissioned satellite from the orbit, the 3,000+ pieces of new MOD particles consequently produced in the test have posed severe HVI risk to other spacecraft, arousing a great deal of controversy from the public [4].

Over the years, NASA and the Department of Defense in the U.S. have been working co-operatively to establish a Space Surveillance Network, aimed at tracking MOD particles that are greater than 5 cm in sizes [5]. With this network, conjunction assessments and collision avoidance maneuvers can be implemented, whereby to counter MOD particles included in the surveillance network. Nevertheless, almost none of the available assessment or avoidance techniques is able to deal with the cases in which MOD particles are smaller than 5 cm [5]. Therefore, prevention of HVI and evaluation of HVI-induced damage, once an attempt to evade MOD particles fails, are the top priority among those endeavors to enhance the survivability, integrity, and durability of space systems, whose importance cannot be overemphasized [2, 6-9].

HVI is significantly different from a low-velocity (several tens meters per second) or high-velocity (up to the order of 10^2 m/s) impact. As a result, the HVI-engendered damage in space structures manifests itself with a high degree of complexity, taking a diversity of modalities due to the much greater kinetic energy that HVI carries and releases during the transient impact. Depending on the size and speed of an MOD particle and the impact location as well, HVI-induced damage can be recrystallization, cell dislocation, micro-cracks, micro-band extension, material vaporization, cratering, spall cracks, plastic zones, and macroscopic penetration or orifices to name a few [1, 2, 10].

To minimize a possible HVI risk to spacecraft, a variety of shielding mechanisms (*e.g.*, Whipple shield [11], stuffed Whipple shield [11], and multi-shock shield [12]) has been designed. A well-installed shielding structure, together with the rear wall of spacecraft, may block an MOD particle with its size not greater than 100 μm (at a normal HVI velocity); but a shielding structure in most instances fails to intercept particles beyond 1 cm [13]. Upon penetration of the outer shielding layer, MOD particles produce shattered debris (forming a debris cloud), to subsequently impinge the inner space structures and cause pitting-like damage scattered chaotically over a large area on the inner structure.

To facilitate the estimation of the residual integrity of the spacecraft upon HVI, the impact location and severity of HVI-caused damage must be evaluated accurately and instantaneously. Based on the evaluation, remedial actions can be applied before the damage reaches a critical level, whereby to prevent an impacted structure from further deteriorating and to weaken the risk of a cascading failure of the entire space system. This is of vital importance and necessity for those spacecraft with long service time or with large surfaces exposed to the space environment. Addressing such significant and imminent needs, several sensing and diagnostic techniques have been deployed, as typified by those using acoustic emissions (AEs) [14, 15], acceleration-based detection [16], thermography [17], calorimetry [18], fiber optic sensor-based detection [19], resistor-based detection [20], microwave emissions, [21] and camera-based surface inspection [22]. All these techniques have been systematically graded by the Inter-Agency Space Debris Coordination Committee [13], in terms of the levels of their respective sensitivity, accuracy, and manipulability, and AE ranked top among all the above mentioned techniques.

Representatively, Forli [14] initiated a series of investigation for the European Space Agency's (ESA) Columbus module (part of the International Space Station) in the early 1990s, to evaluate the feasibility of using an AE-based impact sensor network to detect HVI spots. In the study, twelve bulky AE ultrasonic transducers were used to determine impact localization, with a detection error of approximately 0.4 m. Schäfer and Janovsky [15] attached six bulky ultrasonic transducers onto an aluminum alloy panel and a sandwich panel apiece of Columbus module, via which AE signals during HVI were captured. Conventional triangulation was carried out to locate HVI spots in these two panels, by assuming that HVI-induced waves propagate at a constant velocity throughout the entire panels. Though conducted on ground, these proof-of-concept tests have demonstrated the capability and effectiveness of AE-based detection for locating HVI spots. It is noteworthy that in all these deployments of AE-based detection, the following hypotheses are usually applied:

I. the velocity of HVI-induced wave is constant;
II. there is only one wave mode; and
III. wave dispersion can be largely ignored.

In other words, the difference between HVI and other ordinary impacts (i.e., low- or high-velocity impact) is not a factor to be considered during the previously reported algorithm development for HVI characterization [14, 15].

However, in HVI, shock waves are generated under extreme material compression that behave differently from elastic waves in ordinary impacts. Multiple wave modes co-exist, each featuring a particular velocity, complex dispersive attributes, and severe phase distortion. Together, these effects can obfuscate damage-associated signal features and create vast difficulties in precisely ascertaining the arrival time of AE, accordingly diminishing localization accuracy, provided that a conventional triangulation algorithm is applied with the three hypotheses enumerated above. Prosser *et al.* [23] experimentally examined the AE signals generated in both HVI (1.8~7 km/s) and low-velocity impact (<0.21 km/s) cases, and concluded that the extensional wave modes dominate the signal energy in HVI, whereas the flexural wave modes prevail in low-velocity impact; and compared with low-velocity impact, HVI-induced wave signals feature much larger magnitudes and wider frequency ranges in which the wave energy distributes. This study has revealed that the uniqueness and difference of HVI, compared with other ordinary impacts, shall be addressed towards accurate evaluation of HVI-engendered damage.

Targeting a real time and *in-situ* characterization capacity for real-time awareness of HVI occurrence and accurate evaluation of HVI spots in space shielding structures, the present study is dedicated to fundamental interrogation of HVI-induced AE waves, via numerical simulation and experiment. With the understanding of the unique propagation characteristics of AE waves, an HVI spot in a downscaled two-layer space shielding assembly was located using *in-situ* measured AE waves that were captured with a built-in sensor network comprising miniaturized lead zirconate titanate (PZT) sensing elements. An enhanced, *delay-and-sum*-based imaging algorithm, addressing the difference and uniqueness of HVI compared with other ordinary impacts, was developed for projecting the detected HVI spots into pixelated images. The proposed method in this paper possesses several merits over the others: 1) the miniaturized PZT wafer-formed sensor network endows the monitoring system with an ability of in-situ monitoring of HVI during spacecraft orbiting; 2) quantitative characterization of HVI, including localization of HVI spot, facilities immediate estimate of the severity of HVI-induced damage and offers guide for further repair and replacement; and 3) the proposed imaging algorithm can pinpoint the HVI spot without human intervention or interpretation.

This paper is organized as follows. To begin with, Section 2 describes a dedicated model developed based on three-dimensional smooth-particle hydrodynamics (SPH). With the model, numerical simulation is implemented to depict the unique characteristics of HVI-induced AE waves. Using experiment and numerical modeling, three HVI scenarios are examined in Section 3, in which a projectile, at various impact velocities, impinges a series of shielding assembly of different thicknesses, from normal to oblique impact, and from non-penetration to penetration of the outer shielding layer. The built-in sensor network developed for *in-situ* AE measurements is also illustrated in this section. HVI-generated AE signals, respectively obtained from numerical simulation and from *in-situ* measurements are comparatively analyzed in Section 4. To characterize HVI spots in the shielding layer, a diagnostic imaging approach, originating but enhanced from a *delay-and-sum*-based triangulation method, is developed and elaborated in Section 5, followed by concluding remarks presented in Section 6.

2. Dedicated Modeling of HVI

In pursuit of achieving insight into HVI-induced AE waves and accurate depiction of HVI-generated damage, continued efforts with a nature of theoretical analysis, numerical simulation, or experimental exploration have been made. In such a context, the specific equipment and high testing cost are always a major barrier restricting intensive experimental investigation. Thanks to the bourgeoning computational capacities in recent years, numerical simulation has been increasingly employed to accommodate such a purpose [24-26].

Distinct from low- or high-velocity impacts, HVI features an adiabatic loading process with transient, localized, and extreme material deformation, distortion, melting, and vaporization. This transient loading makes the target structure incapable of reacting in a prompt manner to the impact, leading to the generation of shock waves. As a consequence of large impact forces – much greater than the forces induced in a low- or high-velocity impact, as well as the transient conversion of kinetic to internal energy, the vicinity of an HVI spot usually exhibits material traits between fluid and solid. It would be a daunting task to describe these material traits using conventional numerical methods.

The Eulerian and Lagrangian descriptions [27] are two major theoretical cornerstones, by which the finite difference (FD) and finite element (FE) are respectively governed [23]. However, both FD and FE may encounter bottlenecks when attempting to simulate HVI. That is because FD-based modeling features a fixed spatial grid throughout the entire space, and it can become inefficient due to the singularity in the grid when large deformations under HVI occurs; on the other hand, FE-based modeling may yield erroneous results, because the meshed elements in the vicinity of an HVI spot can be extremely distorted during the impact.

To circumvent the above-stated deficiencies when either FD or FE is used to interpret the material behaviors under HVI, a particle-based Lagrangian algorithm – smooth-particle hydrodynamics (SPH) – has been developed. Initially used for astronomy and then brought to hydrodynamics [28-32], SPH discretizes a modeling domain using mutually un-restricted particles instead of conjointly tied elements, thus allowing excessive deformation of materials with traits between fluid and solid. Nevertheless, up till this moment, most research efforts of using SPH to simulate HVI are limited to the evaluation of structural dynamic responses and resistance to impacts, and there is an obvious lack in using SPH-based approaches to explore HVI-induced AE waves and HVI-engendered damage.

To faithfully delineate the unique and complex material behavior under HVI, a dedicated modeling approach, based on SPH in conjunction with FE, is developed in this study. Although this is a standard SPH development using ANSYS®/Autodyn, the modeling philosophy and methodology can be extended to the simulation and understanding of general HVI. In the approach, SPH discretizes the structure under investigation into particles ($j=1,\cdots,N$), with no fixed connection between any two particles, within a support domain

Ω (a domain of finite size comprised of *N* particles within). Upon discretization, the integral representation of a function $f(\mathbf{x})|_i$ (e.g., material deformation) at particle *i* (denoted by $f(\mathbf{x})|_i$) can be approximated, in terms of $f(\mathbf{x})$ of its neighboring particles, as

$$\begin{aligned} f(\mathbf{x})|_i &= \int_\Omega f(\mathbf{x}')\delta(\mathbf{x}-\mathbf{x}')d\mathbf{x}' \\ &\approx \int_\Omega f(\mathbf{x}')W(\mathbf{x}-\mathbf{x}',h)d\mathbf{x}' \\ &\approx \sum_{j=1}^{N} f(\mathbf{x}_j)W(\mathbf{x}_i - \mathbf{x}_j, h)\Delta V_j \\ &= \sum_{j=1}^{N} f(\mathbf{x}_j)W(\mathbf{x}_i - \mathbf{x}_j, h)m_j / \rho_j, \end{aligned} \tag{1}$$

where ΔV_j, m_j, and ρ_j are the volume, mass, and density of a neighboring particle *j*, respectively. δ is the Dirac delta function, and *W* a smoothing function for approximation. *h* signifies the smoothing length defining the influence area of the smoothing function *W*. Without the fixed connection, the particles adjunct to particle *i* are searched and updated within Ω before each step of calculation using Eq. (1). With a meshless nature and therefore without any geometric constraints, SPH has the potential to be effective in depicting HVI-induced large deformation of material.

The strength of the material is negligible compared with its inertial forces when HVI occurs – a similar behavior to fluids. To reflect such a material attribute, Navier-Stokes equations [33] are recalled in the model, to represent the conservation of mass, momentum, and energy in general hydrodynamics, which reads, in the absence of external forces, as

$$\begin{aligned} \frac{D\rho}{Dt} &= -\rho\frac{\partial v^\alpha}{\partial x^\alpha}, \\ \frac{Dv^\alpha}{Dt} &= \frac{1}{\rho}\frac{\partial \sigma^{\alpha\beta}}{\partial x^\beta}, \\ \frac{De}{Dt} &= \frac{\sigma^{\alpha\beta}}{\rho}\frac{\partial v^\alpha}{\partial x^\beta}, \end{aligned} \tag{2}$$

where α and β $(\alpha,\beta=1,2,3)$ denote tensor indices; ρ, t and e are the density, time and internal energy of an element with infinitesimal volume moving with the flow; and $\mathbf{v}$ (or v^{α}), $\boldsymbol{\sigma}$ (or $\sigma^{\alpha\beta}$) are the velocity vector and stress tensor, respectively; the operator D signifies partial differential in Lagrangian frame.

Stress $\sigma^{\alpha\beta}$ in a projectile and target material consists of two components, namely the isotropic part pressure p and deviatoric part shear stress $\tau^{\alpha\beta}$, as

$$\sigma^{\alpha\beta}=-p\chi^{\alpha\beta}+\tau^{\alpha\beta}, \tag{3}$$

where $\chi^{\alpha\beta}$ signifies the Kronecker delta.

To integrate Navier-Stokes Equation (Eq. (2)) into SPH approximation (Eq. (1)) leads to a set of discretized equations, for particle i over Ω, as

$$\begin{aligned}
&\frac{D\rho_i}{Dt}=\sum_{j=1}^{N}m_j(v_i^{\alpha}-v_j^{\alpha})\cdot\frac{\partial W(x_i-x_j)}{\partial x_i^{\alpha}},\\
&\frac{Dv_i^{\alpha}}{Dt}=\sum_{j=1}^{N}m_j\left(\frac{\sigma_i^{\alpha\beta}}{\rho_i^2}+\frac{\sigma_j^{\alpha\beta}}{\rho_j^2}\right)\cdot\frac{\partial W(x_i-x_j)}{\partial x_i^{\beta}}, \qquad (j=1,\cdots,N)\\
&\frac{De_i}{Dt}=\frac{1}{2}\sum_{j=1}^{N}m_j\frac{p_i+p_j}{\rho_i\rho_j}(v_i^{\beta}-v_j^{\beta})\frac{\partial W(x_i-x_j)}{\partial x_i^{\beta}}+\frac{1}{\rho_i}\tau_i^{\alpha\beta}\dot{\varepsilon}_i^{\alpha\beta},
\end{aligned} \tag{4}$$

where $\dot{\varepsilon}_i^{\alpha\beta}$ denotes the strain rate. Variables in equations for particles i and j are distinguished by the subscripts i and j, respectively. To solve Eq. (4), three groups of supplementary equations, namely (I) equation of state (EOS), (II) strength model, and (III) failure criterion, are introduced into the model [32], whereby the discretized Navier-Stokes equation (Eq. (4)) can be solved numerically with a leapfrog algorithm [34]. In brief, for (I), an EOS describes a correlation between pressure p and the state variables including density ρ and internal energy e. In particular, the shock EOS – a genre of EOS specialized for HVI in which shock waves are generated – is established in this model, based on the Rankine-

Hugoniot jump conditions [35], as well as Mie-Grüneisen equation for solid [36]. For (II), the strength model governs the relationship between shear stress $\tau^{\alpha\beta}$ and strain of the material, indicating yielding conditions of the material under HVI. In this model, the Steinberg Guinan strength model [37], a semi-empirical flow stress model applicable to high strain rates (greater than 10^5 s^{-1}), is adopted. For (III), the failure of the material upon HVI is determined in terms of the selected failure criteria. In this model, the principal tensile stress failure criteria are chosen, which is able to predict material failure when HVI-induced stresses are beyond a pre-defined maximum tensile stress. Aggregating the three groups of supplementary equations with Eq. (4), the HVI problem with extreme material deformation and distortion can be solved, and HVI-induced shock waves can be depicted.

Though effective in delineating an HVI event, the process of searching and updating of neighboring particles at each calculation step using Eq. (1) may incur a high computational cost. On the other hand, during propagation from the impact spot, the HVI-induced shock waves convert quickly to elastic waves in the part of a target structure that is distant from the HVI spot, where material behaves elastically. With the above twofold consideration, SPH-based approach models and simulates HVI-induced shock waves and material deformation within the HVI vicinity only, while FE-based numerical method is used to canvass wave propagation and material deformation beyond HVI vicinity. This leads to a hybrid modeling approach in this study. This hybrid approach is emerging recently and is well validated in terms of its accuracy, as the sole adoption of SPH is often much more CPU consuming compared with SPH-FE approach or may not fulfill the modeling purpose [38, 39]. In this study, it is a good approach achieving an efficient and accurate calculation.

3. Experiment and Simulation

Three sets of downscaled two-layer shielding assembly, simulating a typical space shielding mechanism, were designed and prepared, as shown in **Figure 1**. Each assembly consists of two layers, with the outer layer to be impinged by a projectile first. With a spacing of 150 mm to the outer layer, the inner layer provides a further protection for the inner space structures against HVI in the case that the outer layer is punctured. Both layers are made of aluminum (2024-T4), measuring 600 mm × 500 mm for in-plane dimensions. The three sets of shielding assembly feature two degrees of thickness of the outer layer, in hope of generating different damage: no puncture and puncture cases for the thicker and thinner outer layers, respectively.

With the prepared shielding assembly sets, three HVI scenarios were explored, representing three typical HVI events with various degrees and types of damage induced by HVI:

(I) accelerated to a velocity ~2.5 km/s and impinging the shielding assembly in a normal direction, the projectile (aluminum 2024-T4; Φ3 mm) was blocked by the outer layer with a thickness of 8 mm (no puncture case);

(II) accelerated to a velocity ~4.0 km/s and impinging the shielding assembly in a normal direction, the projectile (aluminum 2024-T4; Φ5 mm) punctured the outer layer with a thickness of 2 mm (puncture case); and

(III) accelerated to a velocity ~4.0 km/s and impinging the shielding assembly in an oblique direction (32^0 with regard to the normal direction of the outer layer), the projectile (aluminum 2024-T4; Φ5 mm) punctured the outer layer with a thickness of 2 mm (puncture case).

In all three scenarios, the thickness of the inner layer of the assembly remained the same (5 mm). Experiment was carried out, followed with numerical simulation using the developed hybrid modeling approach.

3.1. Experiment

The HVI facilities, installed in the State Key Laboratory of Explosion Science and Technology China, were employed for HVI tests. The core equipment of the facilities is a two-stage light gas gun, via which a projectile can be accelerated to impinge a target structure, at a desired velocity up to 10 km/s – the impact velocity in a typical HVI event in the low Earth orbit when an MOD particle collides with a spacecraft. The high-pressure nitrogen gas, filled in the first-stage tube (with a larger cross-section) of the light gas gun, propels the piston to compress the second-stage tube (with a much smaller cross-section) of the gun that is filled with hydrogen gas. Once a pre-set pressure value is met, the hydrogen gas breaks through an aluminum membrane with a pre-made notch, and subsequently a three-pedal sabot with an encapsulated projectile is accelerated to a specific velocity.

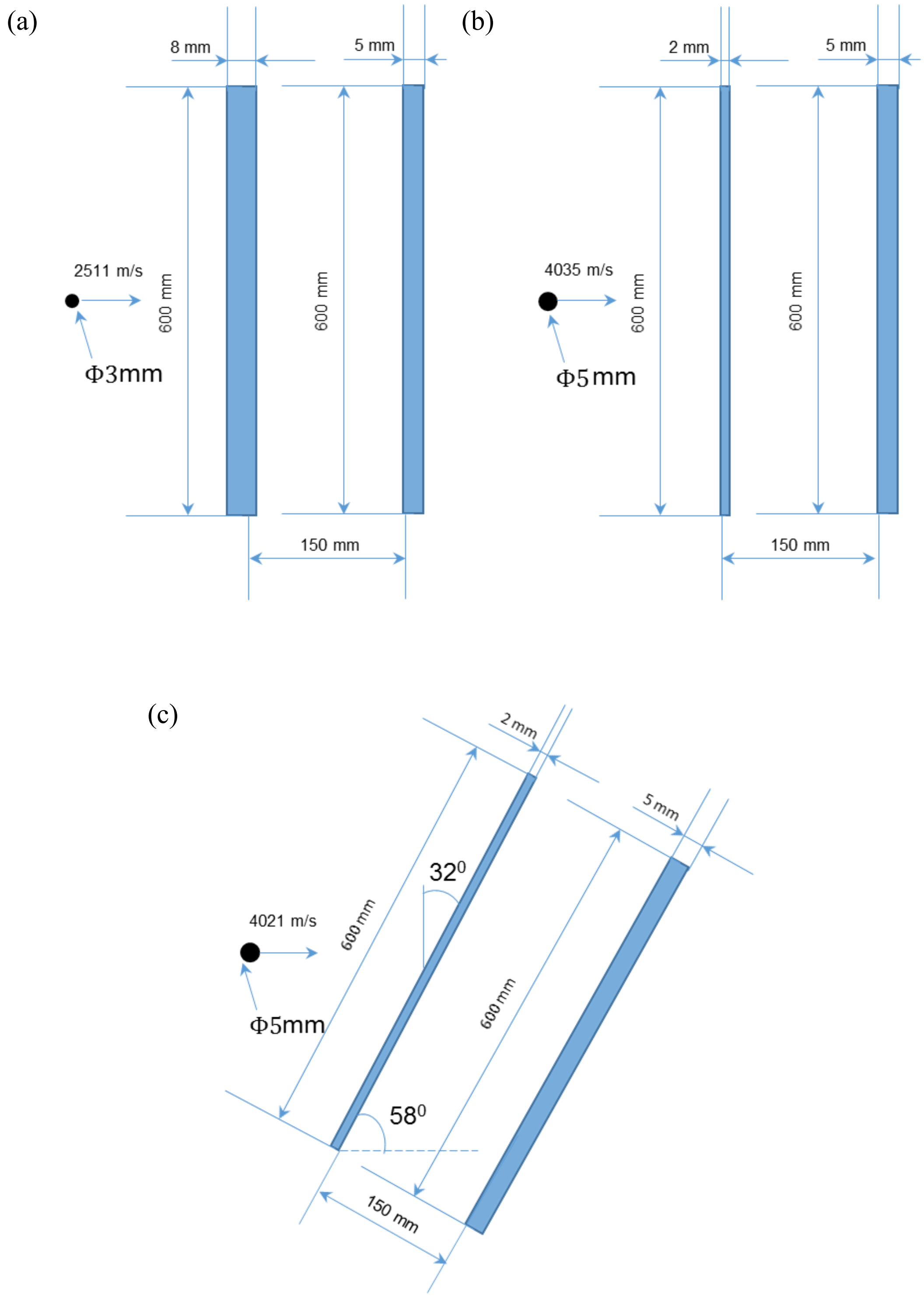

Figure 1 Schematic of three designated HVI scenarios: (a) no puncture of outer layer under normal impact (Scenario I); (b) puncture of outer layer under normal impact (Scenario II); and (c) puncture of outer layer under oblique impact (Scenario III).

Following separation of the projectile from the sabot using a pneumatic separator, the projectile impacts the target structure. The impact velocity is calibrated according to the difference of arrival time between the two magnetic induction coils with a distance of 50 mm in the gas gun. A testing chamber was placed at the end of the gas gun, in which the prepared shielding assembly was immobilized, with different angles of incidence with regard to the projectile, as shown in **Figure 2**.

A built-in sensor network was developed for real-time acquisition of AE signals induced in HVI. Surface-mounted on the outer layer (facing the projectile) using a dual-component adhesive (Pattex®), the sensor network comprised of seven miniaturized and lightweight PZT wafers (Φ8, 0.48 mm thick, denoted by P_i (i = 0, 1, 2, …, 6)). All wafers, along with associated wiring and cabling, were protected using epoxy from detaching from the assembly when HVI occurred. Compared with conventional, bulky AE transducers, PZT wafers used in this study are lightweight and small, rendering a capacity of *in-situ* perception of HVI-induced AE signals. As the thickness of PZT wafer is much smaller compared with the thickness of shielding layer, the PZT wafer dominantly catches the in-plane strain along the direction of wave propagation to represent the AE signals. In Scenario I, seven PZT wafers in the network were positioned in the marginal area near the boundary of the outer layer, as shown in **Figure 3**(a), each of them having the same distance to the anticipated center of the HVI spot; in Scenarios II and III, seven PZT wafers were deployed with various distances to the anticipated HVI spot, ranging from 80 mm to 200 mm with an interval of 20 mm, as shown in **Figure 3**(b). The different locations of the PZT wafers were intended to test the influence of sensor placement on the performance of *in-situ* AE measurements and the robustness of the HVI localization algorithm (to be detailed in Section 5).

(a)

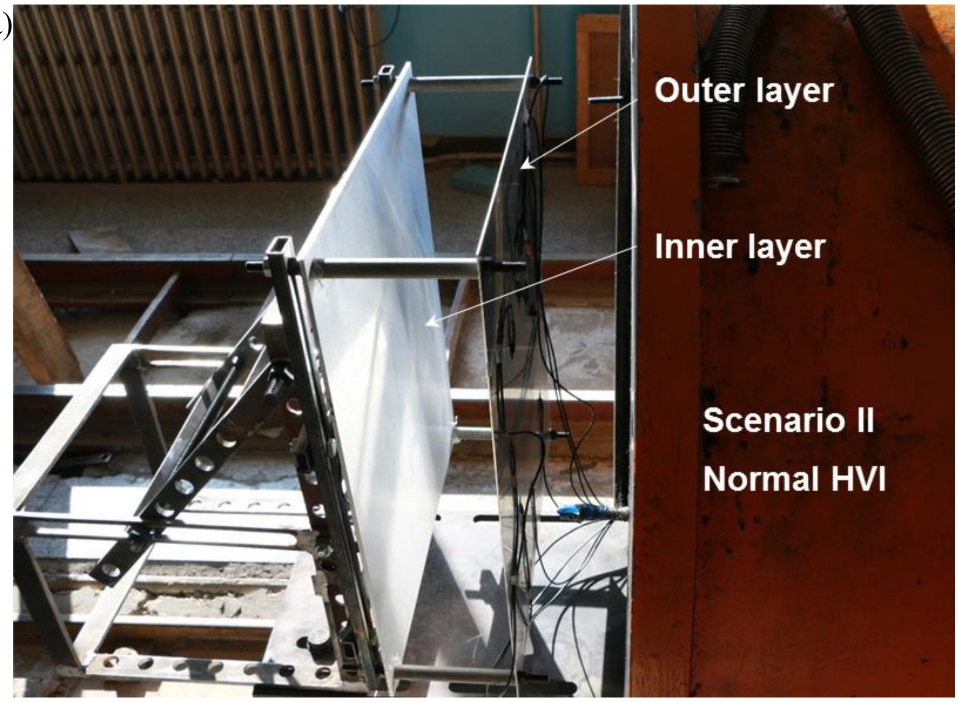

(b)

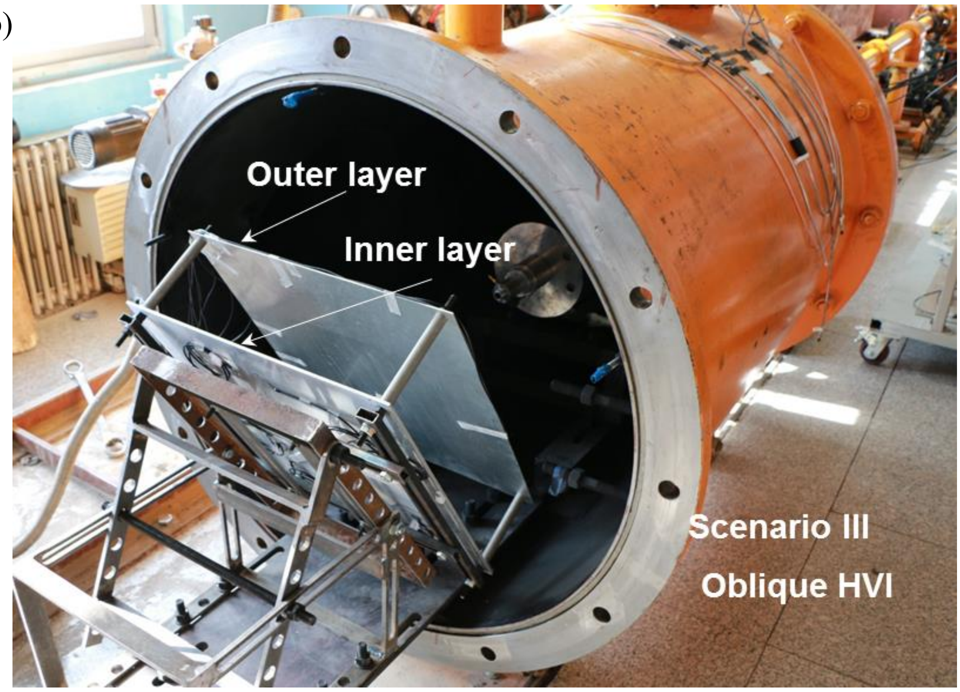

Figure 2 Photographs of the two-layer shielding assembly immobilized in the testing chamber of HVI facilities: (a) for Scenario II (normal impact); and (b) for Scenario III (oblique impact).

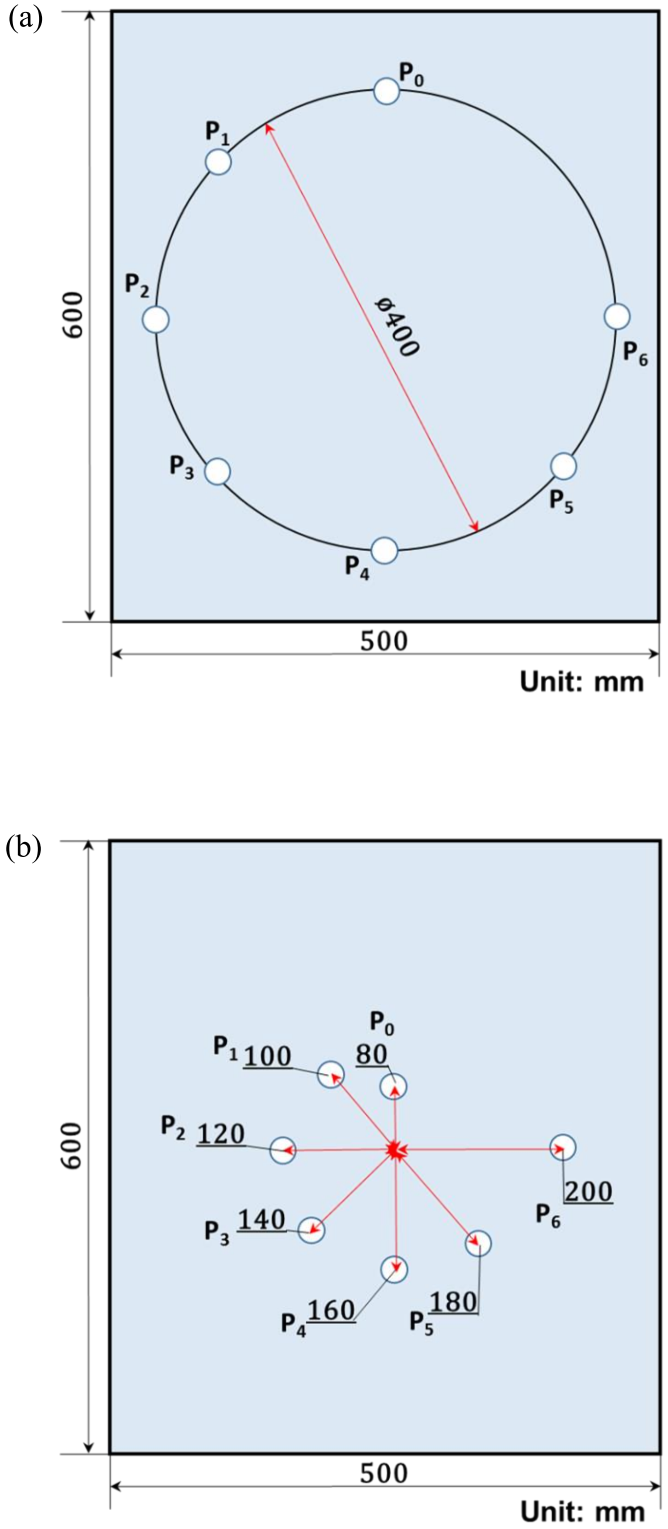

Figure 3 Configurations of the built-in sensor network for *in-situ* AE measurements in (a) Scenario I; and (b) Scenarios II and III.

With the built-in sensor network, AE signals were captured in three designated scenarios, via a self-contained signal acquisition system developed on a PXI (PCI eXtensions for Instrumentation) bus platform (NI® PXIe-1071). The schematic of the test, along with the signal acquisition system, is shown schematically in **Figure 4**.

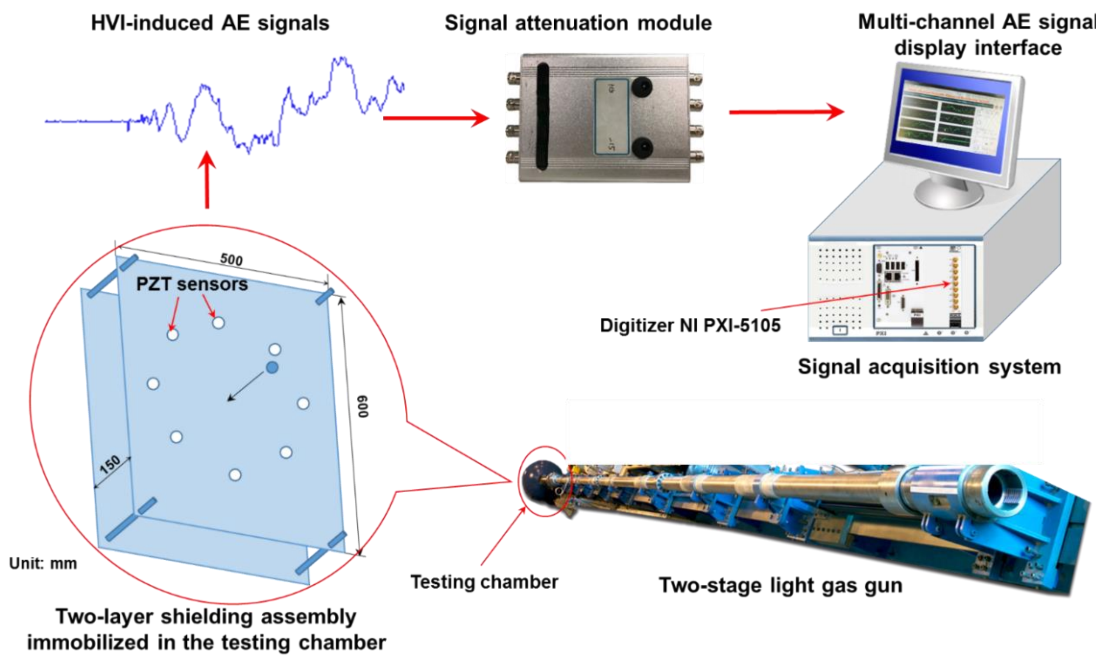

Figure 4 Schematic of experimental set-up.

Table 1 lists the key parameters of tests and consequences of each impact. During *in-situ* measurements, the kinetic energy induced by the vast shock energy deformed the target structure to hundreds of microstrain, and the magnitudes of captured AE signals were in most circumstances out of the measurement range of the signal acquisition system. A signal attenuation module was developed and included in the system, to attenuate captured AE signals by 15 times. Upon attenuation, AE signals were registered with an eight-channel digitizer (NI® PXI-5105). A trigger voltage of 1 V on the attenuated signal acquired with sensor P_0 (see Figure 3) was applied, to synchronize AE signal acquisition by the remaining PZT sensors in the sensor network.

Table 1 Key parameters of tests and consequences of each impact

Scenario	Projectile diameter (mm)	Velocity (km/s)	Impact type	Outer layer thickness (mm)	Inner layer thickness (mm)	Consequence (for outer layer)
I	3	2.511	normal	8	5	not punctured
II	5	4.035	normal	2	5	punctured
III	5	4.021	oblique (32^0)	2	5	punctured

3.2. Simulation

Pursuant to experiments, numerical simulations were implemented on ANSYS®/Autodyn platform using the developed hybrid SPH-FE modeling approach. Three models were respectively developed, in accordance with the three scenarios of the experiment.

By way of illustration, Figure 5(a) shows the sketch of the developed hybrid model for Scenarios II (normal incidence) and III (oblique incidence). For Model I, the only difference is that the outer layer has a thickness of 8 mm. In the three models, a symmetric boundary condition was applied at the symmetric plane x-z of the outer layer and the projectile as well. The vicinity of the HVI spot was determined using the model to be 50 mm × 25 mm on the target structure, as shown in the insert of Figure 5(a). The criteria for the size of SPH area is mainly based on the estimated area of crater size. It is generally deemed that the crater is formed as a result of large plastic deformation, which can be modeled using SPH. According to [2], the ratio of a crater size to the projectile diameter can be expressed via an empirical equation as

$$D_c / d_p = 1.1(\rho_p / \rho_t)^{1/3}(\rho_t / \sigma_t)^{1/3}(v_t / v_p)^{1/3} u_0^{2/3}(1+\rho_p / \rho_t)^{2/3}, \tag{5}$$

where d_p is the projectile diameter, and D_c the crater diameter. ρ_p and ρ_t are the projectile and target densities, respectively. u_0 is the projectile (impact) velocity. v_t and

v_p are the target and projectile bulk sound velocities, respectively. σ_t is the target (static) yield strength. Here, using $\rho_p / \rho_t = 1$, $\rho_t = 2783\text{kg/m}^3$, $\sigma_t = 324\text{MPa}$ [40], v_t / v_p =1, and $u_0 \approx 4000\text{m/s}$ in the model, D_c / d_p is calculated to be ~9 according to Eq. (5). Thus in Scenarios 2 and 3, D_c is approximately nine times the diameter of the projectile (5 mm), which is ~45 mm. The determined vicinity with a size of 50 mm × 25 mm has been demonstrated sufficient to include the region in which the material of the shielding layer behaves plastically and HVI-induced shock waves fully convert to elastic waves. The vicinity of HVI spot, together with half the sphere projectile, was simulated using SPH-based modeling; while the rest of the shielding layer was meshed using FE-based modeling. In FE, a uniform element length of 0.5 mm was allocated, based on the criterion that at least ten nodes should be allocated per wavelength, which is ~6.2 mm in the context of 1 MHz and ~6200 m/s for the concerned maximum frequency and bulk wave velocity, respectively. The particle was allocated in the size of 0.2 mm which has been demonstrated sufficient to achieve satisfactory simulation precision. With these settings, the energy deviation was controlled to be < 5%, well guaranteeing simulation accuracy, as shown in Figure 5(b). To link the two parts that were respectively modeled using SPH and FE, a tie-type bonding condition, as an enforced coincidence of displacement in the whole process of calculation, was applied at the interface between SPH particles and FE nodes. For comparison with experimental results, in-plane (y-z) strains along the wave propagation direction were extracted from those FE nodes at the locations where PZT wafers were positioned in experiment. Taking one node with an angle of θ with regard to z axis as an example, the in-plane strain (referring to Figure 5 (a)) is expressed as

$$\varepsilon = \varepsilon_z \cos^2\theta + \varepsilon_y \sin^2\theta + 2\varepsilon_{zy} \sin\theta\cos\theta, \tag{6}$$

where ε_z, ε_y and ε_{zy} are the normal strains along the *z* axis, along the *y* axis, and shear strain in the *y*-*z* plane, respectively.

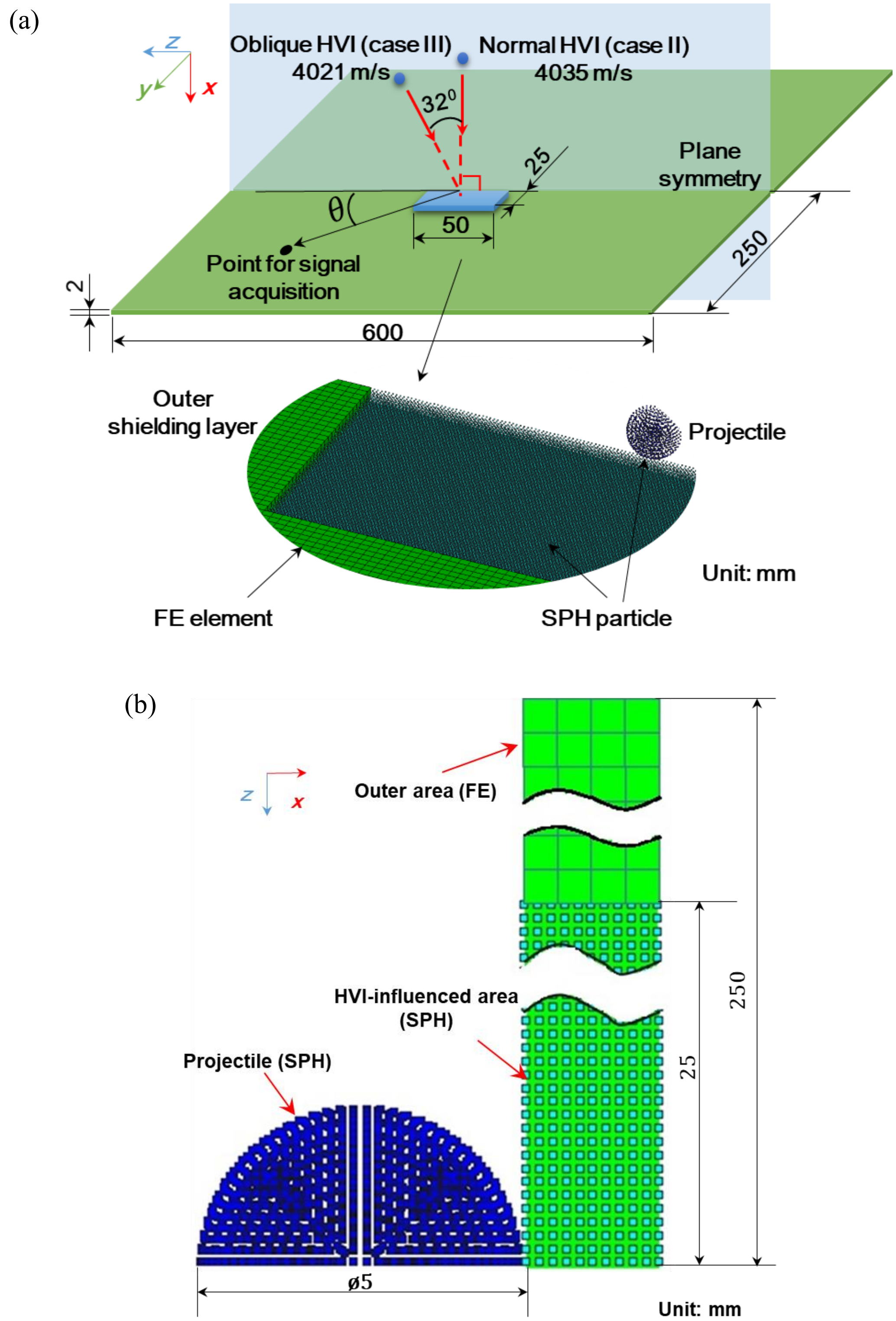

Figure 5 (a) Sketch of developed hybrid model for Scenario II (normal incidence) and III (oblique incidence); and (b) sectional view of the model, showing particles in the HVI

vicinity (using SPH) and elements in the rest of the shielding layer (using FE).

The key material properties of the projectile and target structures used in the simulation are listed in **Table 2**. As illustrated in Section 2, the Shock EOS, Steinberg Guinan strength model, and principal tensile stress failure criteria were adopted in SPH-based modeling. In particular for the failure criteria, 469 MPa [40] was the threshold for both the projectile and target structures, beyond which material failure was anticipated.

Table 2 Material properties of projectile and target structure used in simulation

Parameter		**Parameter**	
Equation of state (Shock)		**Strength model (Steinberg Guinan)**	
Density ρ_0	2.785(g/cm^3)	Shear modulus G_0	28.6 GPa
Gruneisen coefficient Γ	2	Yield Stress Y_0	260 MPa
Parameter c_0	5382(m/s)	Maximum Yield Stress Y_{max}	760 MPa
Parameter s	1.338	Hardening constant	310
Reference temperature T_0	300 K	Hardening exponent	0.185
Specific heat C_v	863 J/kgK	Derivative dG/dP	1.8647
Failure		Derivative dG/dT	-17.62 (MPa/K)
(Principal stress)	469 MPa	Derivative dY/dP	0.01695
		Melting temperature T_{melt}	1220 K

4. Analysis and Comparison

In both experiments and simulations, HVI-induced AE waves were acquired, and the consequences of each impact were analyzed comparatively.

4.1. Experimental Results

HVI-induced damage in the outer shielding layer in the three designated scenarios is shown in **Figure 6**, showing different degrees of damage, subjected to the impact velocity and incident angle of the projectile.

(a)

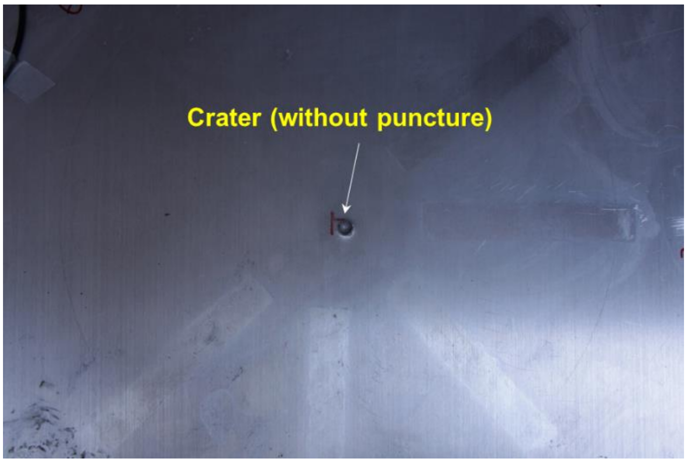

(b)

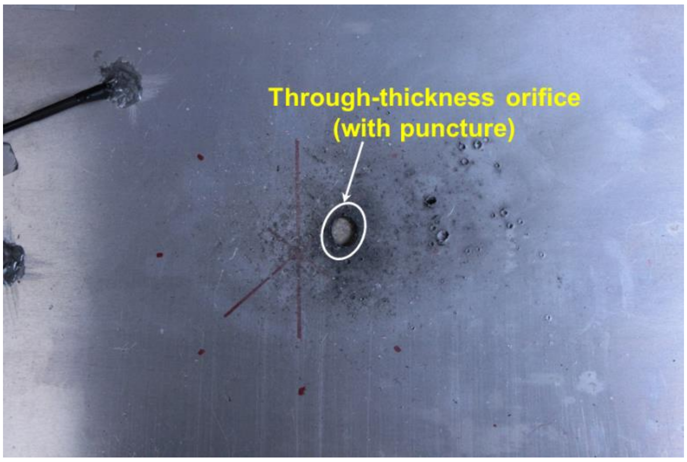

(c)

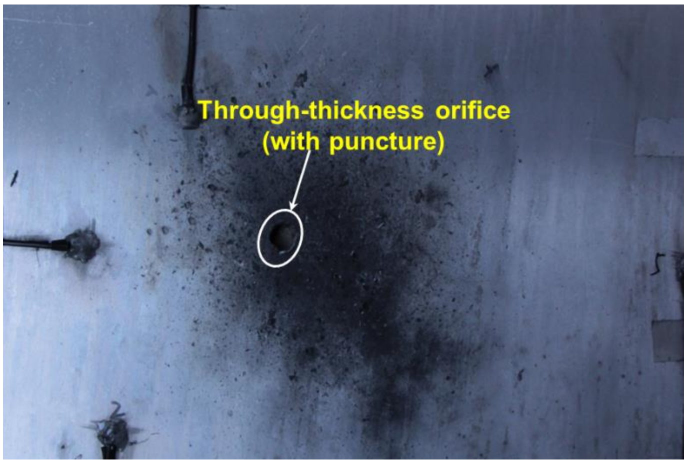

Figure 6 HVI-engendered damage in the shielding layer in Scenarios (a) I; (b) II; and (c) III.

By way of illustration, **Figure 7**(a) displays the AE signals experimentally acquired with P_2 in Scenario II, to observe a conspicuous high-frequency wave component – the first-arrival wave in the signal – followed with a series of low-frequency wave components. These wave components are the elastic waves that are converted from the HVI-induced shock waves. According to the calculated wave propagation velocity, the high-frequency first-arrival wave component is the fundamental symmetric Lamb wave (S_0) guided by the outer layer of the shielding assembly, and the low-frequency wave components are a mixture of the fundamental anti-symmetric Lamb wave (A_0) and low-frequency vibration of the assembly. The spectra of the acquired signals were obtained via a Fast Fourier Transform (FFT), and the one for the signal shown in **Figure 7**(a) is exhibited in (b), in which the low-frequency power represents the low-frequency wave mixture.

To analyse signals more explicitly, a second order high-pass Butterworth filter with a cutoff frequency of 5 kHz was applied to all captured signals to screen the low-frequency structural vibration, leaving only S_0 mode and A_0 mode in the filtered signals. With a much faster propagation velocity compared to A_0 mode, S_0 mode arrives first. In addition, the magnitude of S_0 mode is greater than that of A_0 mode, leading to a higher signal-to-noise ratio. For these reasons, S_0 mode, converted from the HVI-induced shock waves, was used for locating the HVI spot in the subsequent section.

(a)

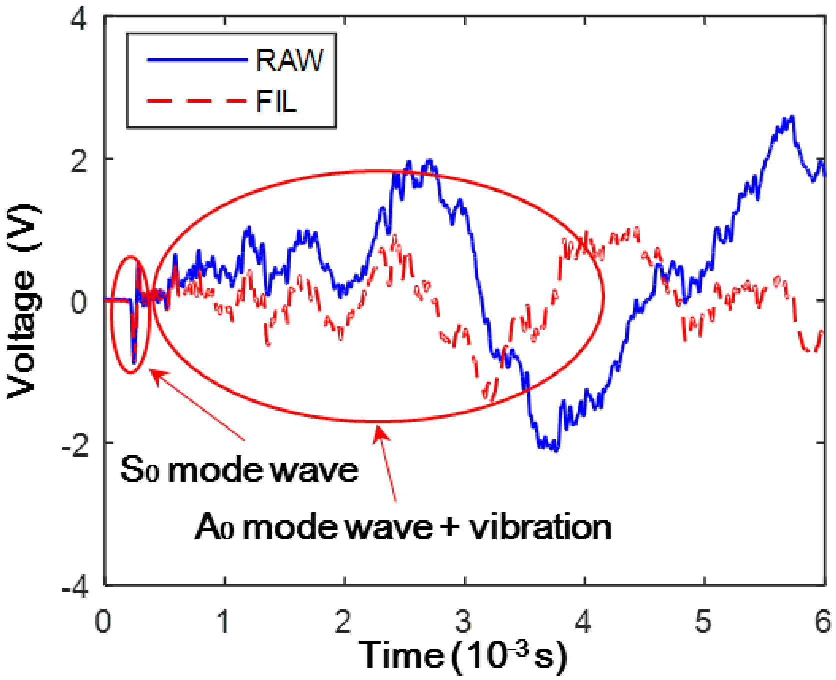

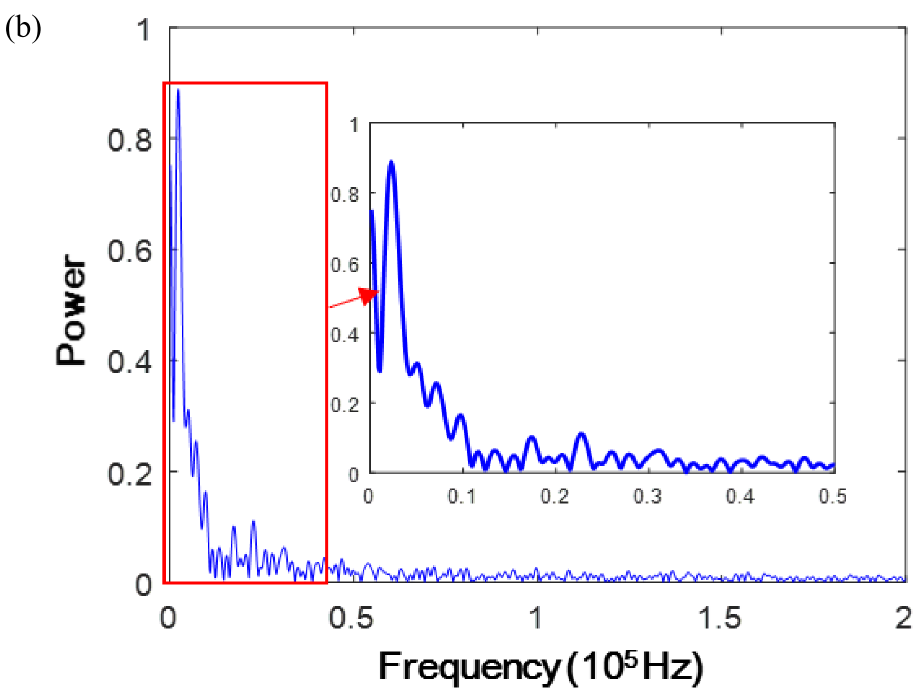

Figure 7 Signal experimentally acquired with sensor P_2 in Scenario II: (a) raw (upon signal attenuation) and filtered signals; and (b) signal spectra (RAW – raw but attenuated signal, FIL - filtered signal with a high pass filter of 5 kHz).

4.2. Simulation Results

Continuing to use Scenario II as the example, the in-plane strains were extracted from the FE nodes at the location where P_2 was positioned in the experiment, as shown in **Figure 8**(a). With the simulation, it is possible to acquire strains at two points respectively on the upper and lower surfaces of the shielding layer that share the same in-plane positions, this allowing to isolate symmetric (corresponding to S_0) and anti-symmetric (corresponding to A_0) strain components from raw signals using a simple addition and subtraction manipulation of the two strain signals. With this manipulation, the ascertained results for the signals in **Figure 8**(a) are shown in (b). Comparing **Figures 8**(b) against 7(a), it can be noted that the filtered signals in the experiment are consistent with the processed signals of the simulation, in terms of the arrival time and waveform of the first-arrival wave component (S_0).

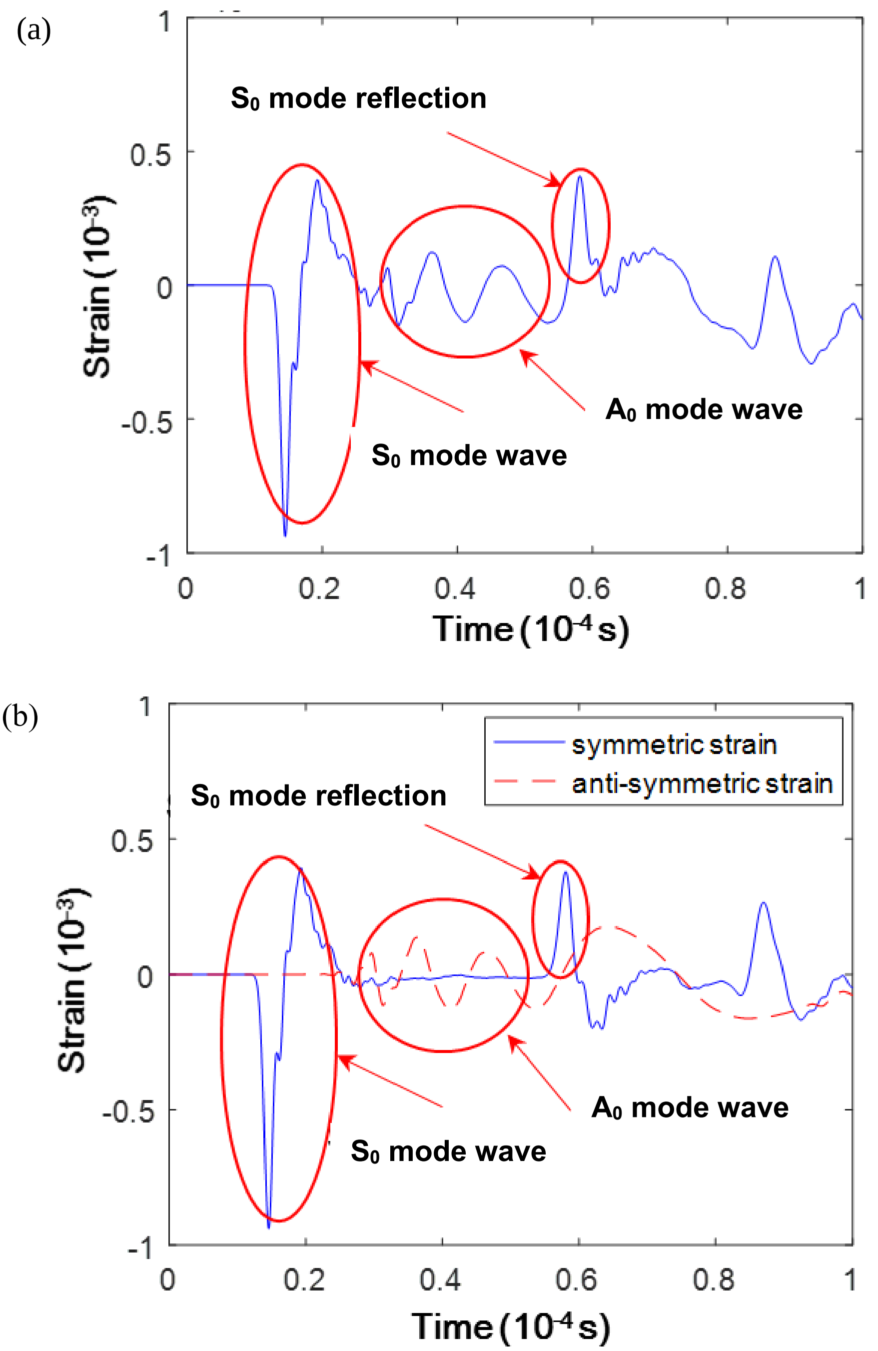

Figure 8 Signals in simulation acquired with sensor P_2 in Scenario II: (a) raw strain signal; and (b) isolated symmetric (corresponding to S_0) and anti-symmetric (corresponding to A_0) strain components.

4.3. Comparison

To validate the developed hybrid model, signals obtained in simulation were normalized with regard to the magnitude of S_0 mode and then compared with the signals obtained with the experiment. Without loss of generality, **Figure 9**(a) compares the signal experimentally captured at P_2 in Scenario II against its corresponding signal obtained in simulation, to observe a qualitative agreement in between. In the experimental signal, the structural vibration-related signal components are prominent, which the simulation cannot capture well, because the four-edge-fixed boundary conditions in the simulation are substantially different from the constraints in the experiment. Taking a step further, upon the signal filtering (with a high pass filter of 5 kHz) to remove low-frequency vibration components, the simulation and experimental signals are in good accordance, as shown in **Figure 9**(b).

(a)

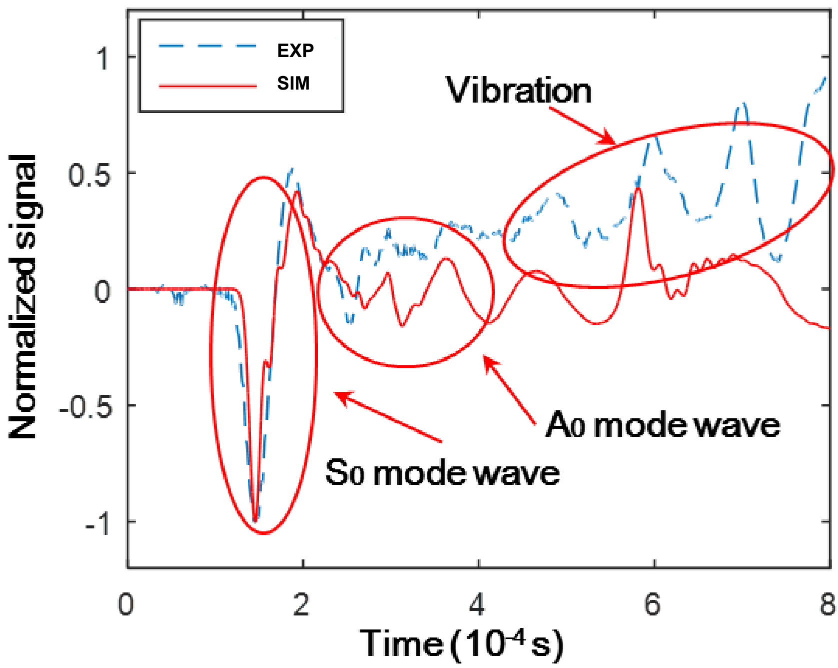

(b)

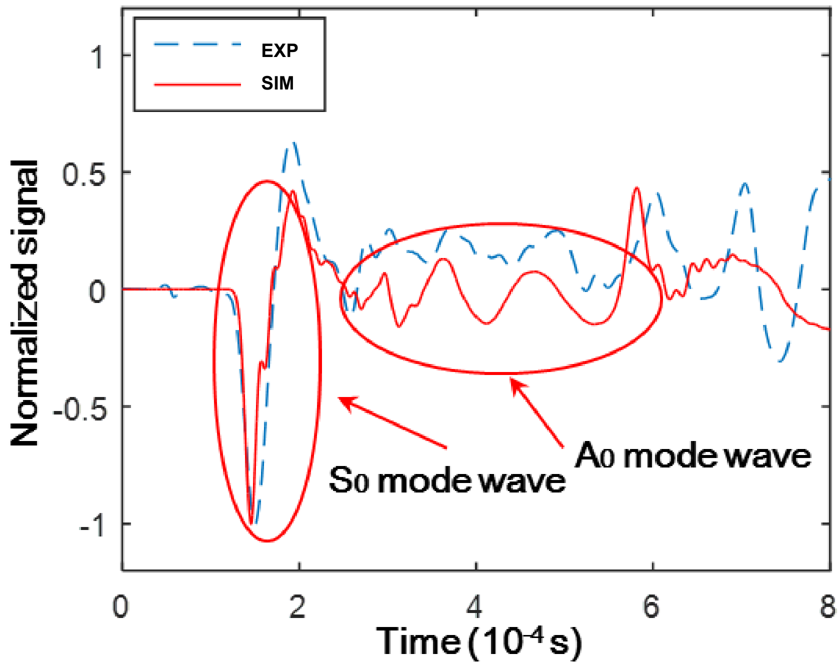

Figure 9 Comparison of simulation and experimental results (for Scenario II, captured by sensor P_2): (a) raw; and (b) filtered signals (EXP - experimental signal, SIM – simulation signal).

A further analysis of the dynamic responses of the outer shielding layer under HVI was performed, to gain insight into the sources of various wave components included in captured AE signals. Based on the hydrodynamics theory described in Eq. (3), the HVI-induced stresses basically feature a dominant hydrostatic stress (pressure), as well as a weak shear stress. Shock waves are generated due to the drastic pressure rise, provided that the outer layer is unable to absorb the kinetic energy of the HVI. Meanwhile, the weak shear waves are also generated due to the shear stress. The dominant lateral shock waves, along with the shear waves, scatter from the central HVI spot and then convert into elastic guided waves composed of symmetric and anti-symmetric modes in the elastic area of the shielding layer. Among the elastic guided waves, S_0 retains most of the energy from the lateral shock wave, which is the theoretical foundation to interpret the observation in both simulation and experiment that the S_0 mode dominates the signal energy over the A_0 mode. In addition, as observed in both experimental and simulation results (**Figures 7-9**), the S_0 mode, compared with the A_0 mode, features faster propagation velocity, larger magnitude, and less dispersion. All these traits of S_0 can facilitate the characterization of HVI-induced damage in the shielding assembly.

5. Localization of the HVI Spot

5.1. Principle

Based on the understanding of propagation characteristics of HVI-induced AE waves via both experiment and simulation, a real time, *in-situ* AE-based characterization framework for HVI was subsequently developed. 'Real time and *in-situ*' gives the framework the potential to sense in real time and characterize HVI without down time or disassembly. Thus, once HVI occurs, the developed framework can immediately identify the location of HVI, estimate the severity of HVI-induced damage, and further guide the action of repair. An enhanced, *delay-and-sum*-based diagnostic imaging algorithm was proposed and included in the framework, whereby identified HVI damage in the shielding layer can be visualized.

In the algorithm, assuming the HVI spot is at point (y, z) on the outer layer of the shielding assembly, the time delay in the arrival of the first-arrival wave (i.e., S_0, as interpreted earlier) captured with any two PZT sensors of the sensor network ((P_i (i = 0, 1, 2, …, 6))), say P_i at (y_i, z_i) and P_j at (y_j, z_j), can be expressed as [41]

$$
\begin{aligned}
\Delta t &= t_i - t_j = (t_0 + t_{shock-i} + \Delta t_i) - (t_0 + t_{shock-j} + \Delta t_j) \\
&= \frac{(\Delta d_i - \Delta d_j)}{v_{plate}} + \int \frac{dr_i}{v_{shock-i}} - \int \frac{dr_j}{v_{shock-j}} \\
&= \frac{(\sqrt{(y-y_i)^2 + (z-z_i)^2} - r_i) - (\sqrt{(y-y_j)^2 + (z-z_j)^2} - r_j)}{v_{plate}} + \int_0^{r_i} \frac{dr_i}{v_{shock-i}} - \int_0^{r_j} \frac{dr_j}{v_{shock-j}} \\
&\approx \frac{(\sqrt{(y-y_i)^2 + (z-z_i)^2}) - (\sqrt{(y-y_j)^2 + (z-z_j)^2})}{v_{plate}}.
\end{aligned}
\tag{7}
$$

Variables in Eq. (7) are discriminated by subscripts i and j for two PZT sensors. t_0 signifies a reference time upon the impact occurrence on the outer layer. For sensor P_i, $t_{shock-i}$ and $v_{shock-i}$ are the duration and speed of HVI-induced shock waves propagating from the HVI spot to the perimeter of the region within which the shielding material is extremely and transiently compressed under HVI (this area is termed "***HVI-influenced area***" hereinafter); Δt_i denotes the subsequent duration when S_0 mode, converted from shock waves, propagates from the perimeter of the HVI-influenced area to P_i. v_{plate} denotes the propagation velocity of S_0 mode outside the HVI-influenced area. r_i and Δd_i are the distances along which the wave propagation takes the modality of shock wave (with a velocity of $v_{shock-i}$) and the form of S_0 (with a velocity of v_{plate}), respectively.

Notably, in the HVI-influenced area, $v_{shock-i}$ decreases along the wave propagation. It is noteworthy that in an oblique HVI, the material compression and deformation are distinct in different wave propagation directions. This wave propagation anisotropy is reflected in the integral terms with regard to $v_{shock-i}$ in Eq. (7). As demonstrated earlier [41], this anisotropy only exerts a minute influence on the propagation of shock waves and would not incur marked error in locating the HVI spot.

Mathematically, Eq. (7) represents a locus that the difference between two distances – the one from the impact point (y, z) to sensor P_i at (y_i, z_i) and the one from the impact point to sensor P_j at (y_j, z_j) – is a constant, *i.e.*, a set of hyperbolas with P_i and P_j being its two foci. Using a diagnostic *delay and sum*-based imaging approach based on the above principle described by Eq. (7) [42-46], the outer layer of the shielding assembly can be mapped into a two-dimensional pixelated image, in which the pixel value at each pixel reflects the probability of an HVI spot therein. In analogy to this, any two PZT wafers in the sensor network form a sensor pair, and create a two-dimensional color-scale synthetic image. All the pixel values calculated with the same Δt are located on the same hyperbola. Based on the principle of *delay and sum*, summing the images rendered by all sensor pairs in the sensor network yields a superimposed image (*ultimate resulting image* in what follows) - a collective consensus as to HVI from the entire sensor network.

5.2. Results and Discussions

With the imaging algorithm, HVI spots on the outer shielding layer in three designated HVI scenarios were located using *in-situ* measured AE signals obtained from experiments, as shown in **Figure 10**. In particular, the images constructed with raw signals are shown in **Figure 10**(a) ~ (c), which, however, fail to pinpoint any HVI spot. The reason can be attributed to the fact that the first-arrival S_0 modes are overwhelmed by vibration-related low-frequency wave components, leading to marked error. To circumvent the interference from A_0 mode and other vibration-related signal components, a high-pass filter with a cut-off frequency of 40 kHz was applied to the raw signals. The accordingly constructed images with noise-filtered signals are displayed in **Figure 10**(d) ~ (f)), showing clear and focused HVI spots.

It is noteworthy that in Scenario I, the sensors were placed near the structural boundary (see **Figure 3**(a)), and therefore, in the simulation the boundary-reflected S_0 modes are prone to be mixed with the first-arrival S_0 modes in Scenario I compared with Scenarios II and III. This mixing degrades the extraction of the accurate arrival time of first-arrival S_0, leading to a pseudo spot (**Figure 10**(d)) to be identified. In addition, even though HVI spots in Scenarios II and III are highlighted in **Figure 10**(e) and (f) with noise-filtered signals, the detection accuracy and image focusing are still inferior, due to the interference from the S_0 modes reflected from the structural boundary in the simulation. To this end, a screening approach was recalled to exclude boundary reflections from the signals, and the consequently constructed images, **Figure 10**(g) ~ (i), show further enhanced accuracy and focusing.

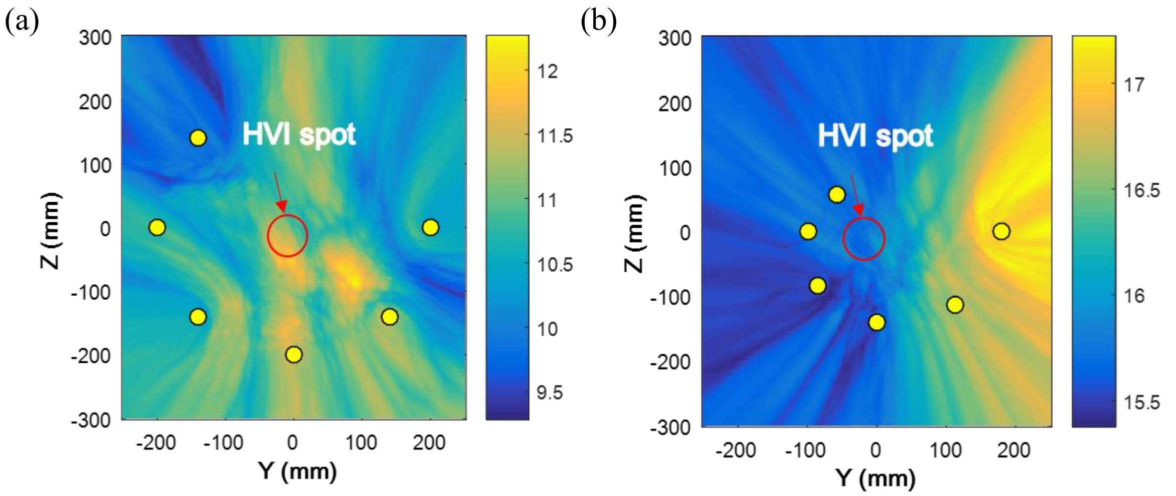

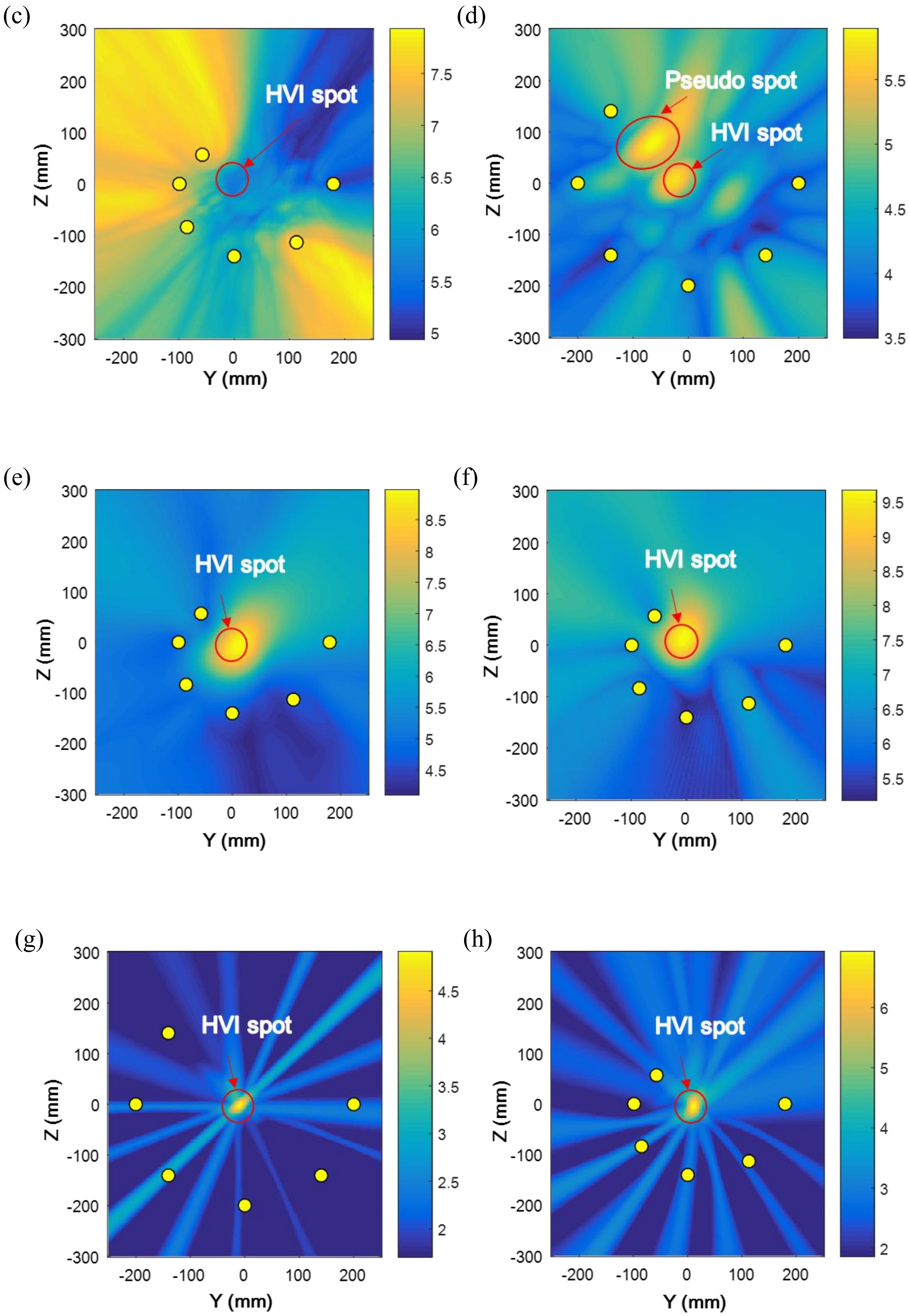
(c)
HVI spot
Z (mm)
Y (mm)
(d)
Pseudo spot
HVI spot
Z (mm)
Y (mm)
(e)
HVI spot
Z (mm)
Y (mm)
(f)
HVI spot
Z (mm)
Y (mm)
(g)
HVI spot
Z (mm)
Y (mm)
(h)
HVI spot
Z (mm)
Y (mm)

(i)

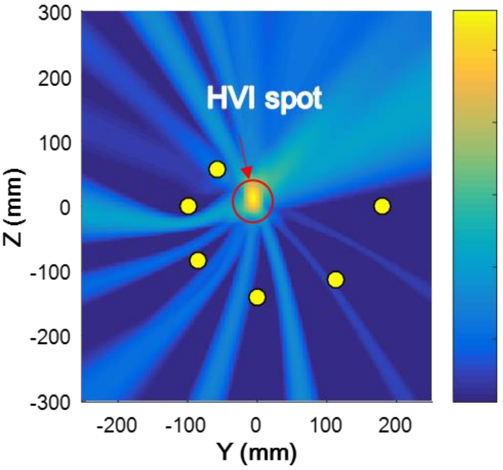

Figure 10 Diagnostic images using *in-situ* measured AE signals for (a) Scenario I using raw signals; (b) Scenario II using raw signals; (c) Scenario III using raw signals; (d) Scenario I using noise-filtered signals; (e) Scenario II using noise-filtered signals; (f) Scenario III using noise-filtered signals; (g) Scenario I using noise-filtered and reflection-screened signals; (h) Scenario II using noise-filtered and reflection-screened signals; and (i) Scenario III using noise-filtered and reflection-screened signals.

6. Concluding Remarks

The threat of HVI to orbiting spacecraft has been of great concern. Significantly different from other ordinary impacts, HVI features a transient loading process with localized, and extreme material deformation, distortion, and melting. In this study, HVI-induced AE waves and HVI-caused damage were studied numerically and experimentally. Using a series of downscaled two-layer shielding assembly, different impact velocities and shielding layer thicknesses were examined under normal and oblique impacts. A dedicated, hybrid modeling and simulation approach was developed, by integrating particle-based SPH and element-based FE, which has been experimentally demonstrated to be accurate in depicting HVI-induced AE signals. In this experiment, lightweight and miniaturized PZT wafers were networked to perceive HVI-generated AE waves in an *in-situ* manner. Analysis of signals in the time and frequency domains have revealed that multiple wave modes, together with structural vibration, co-exist in captured AE signals, entailing appropriate signal processing and screening. An enhanced, *delay-and-sum*-based imaging algorithm was developed, capable of visualizing HVI spots in a pixelated image. This algorithm is capable of localizing HVI even though the sensors are placed far over 200 mm from the HVI spot. It is the dimension of the cavity in the two-stage light gas gun that limits the dimensions of the shielding layer and the sensor placement. The magnitudes of captured AE signals were in most circumstances out of the measurement range of the signal acquisition system, such that a signal attenuation module has to be designed, which implies that the maximum monitoring area can be much larger compared with the reported one. Combining theoretical analysis, numerical modeling, experimental validation, imaging algorithm, and built-in sensor network approach, this study has demonstrated an *in-situ* AE-based characterization framework towards HVI. The ratio of the amplitude between different wave components is to be analyzed, to try to determine if the shielding layer is punctured or not. The additional penalty brought to spacecraft by the HVI characterization system, including weight, size, and power, should be the primary concern to make this method useful to space engineering.

Acknowledgments

This project is supported by the Hong Kong Research Grants Council via General Research Funds (No. 15201416 and No. 15214414). This project is also supported by National Natural Science Foundation of China (Grant No. 11521062). The authors are grateful to Dr. Qiang Wu for his support during HVI tests.

References

1. Ramjaun, D., et al., *Hypervelocity impacts on thin metallic and composite space debris bumper shields.* AIAA journal, 2003. **41**(8): p. 1564-1572.
2. Murr, L.E., et al., *The low-velocity-to-hypervelocity penetration transition for impact craters in metal targets.* Materials Science and Engineering: A, 1998. **256**(1–2): p. 166-182.
3. NASA Orbital Debris Program Office, *Monthly Number of Objects in Earth Orbit by Object Type.* Orbital Debris Quarterly News, 2016. **20**(1&2): p. 13-13.
4. Reichhardt, T. *Satellite Smashers. Space-faring nations: Clean up low Earth orbit or you're grounded.* 2008; Available from: http://www.airspacemag.com/space/satellite-smashers-25098285/?all.
5. NASA. *Space Debris and Human Spacecraft*. 2013 27 September 2013]; Available from: http://www.nasa.gov/mission_pages/station/news/orbital_debris.html.
6. See, T., et al., *Meteoroid and debris impact features documented on the long duration exposure facility*. 1990, DTIC Document.
7. Baluch, A.H., Y. Park, and C.G. Kim, *Hypervelocity impact on carbon/epoxy composites in low Earth orbit environment.* Composite Structures, 2013. **96**: p. 554-560.
8. Drolshagen, G., *Impact effects from small size meteoroids and space debris.* Advances in Space Research, 2008. **41**(7): p. 1123-1131.
9. Christiansen, E., J. Hyde, and R. Bernhard, *Space Shuttle debris and meteoroid impacts.* Advances in Space Research, 2004. **34**(5): p. 1097-1103.
10. Razzaqi, S.A. and M.K. Smart, *Hypervelocity Experiments on Oxygen Enrichment in a Hydrogen-Fueled Scramjet.* AIAA journal, 2011. **49**(7): p. 1488-1497.
11. Christiansen, E.L., *Design and performance equations for advanced meteoroid and debris shields.* International Journal of Impact Engineering, 1993. **14**(1): p. 145-156.
12. Cour-Palais, B.G. and J.L. Crews, *A multi-shock concept for spacecraft shielding.* International Journal of Impact Engineering, 1990. **10**(1): p. 135-146.
13. Inter-Agency Space Debris Coordination Committee WG3, *Sensor Systems to Detect Impacts on Spacecraft*. 2013.
14. Forli, O., *In orbit in-service inspection.* ESA, Space Applications of Advanced Structural Materials p 157-161(SEE N 91-11812 03-24), 1990.
15. Schäfer, F. and R. Janovsky, *Impact sensor network for detection of hypervelocity impacts on spacecraft.* Acta Astronautica, 2007. **61**(10): p. 901-911.
16. Pavarin, D., et al., *Acceleration fields induced by hypervelocity impacts on spacecraft structures.* International Journal of Impact Engineering, 2006. **33**(1–12): p. 580-591.
17. Howell, P., W. Winfree, and K.E. Cramer. *Infrared on-orbit inspection of shuttle orbiter reinforced carbon-carbon using solar heating*. in *Optics & Photonics 2005*. 2005. International Society for Optics and Photonics.
18. Kobusch, M., et al. *Calorimetric energy detector for space debris*. in *Paper IAC-06-B6. 3.9, 57th International Astronautical Congress*. 2006.
19. Staszewski, W., C. Boller, and G.R. Tomlinson, *Health monitoring of aerospace structures: smart sensor technologies and signal processing*. 2004: John Wiley & Sons.
20. Fukushige, S., et al., *Development of perforation hole detection system for space debris impact.* International journal of impact engineering, 2006. **33**(1): p. 273-284.
21. Starks, M., et al., *Seeking radio emissions from hypervelocity micrometeoroid impacts: Early experimental results from the ground.* International journal of impact

engineering, 2006. **33**(1): p. 781-787.

22. Hirayama, H., T. Hanada, and T. Yasaka, *In situ debris measurements in MEO/HEO using onboard spacecraft surface inspection system.* Advances in Space Research, 2004. **34**(5): p. 951-956.
23. Prosser, W.H., M.R. Gorman, and D.H. Humes, *Acoustic emission signals in thin plates produced by impact damage.* Journal of Acoustic Emission, 1999. **17**: p. 29-36.
24. Hiermaier, S., et al., *Computational simulation of the hypervelocity impact of Al-spheres on thin plates of different materials.* International Journal of Impact Engineering, 1997. **20**(1): p. 363-374.
25. Riedel, W., S. Hiermaier, and K. Thoma, *Transient stress and failure analysis of impact experiments with ceramics.* Materials Science and Engineering: B, 2010. **173**(1–3): p. 139-147.
26. Ma, S., X. Zhang, and X.M. Qiu, *Comparison study of MPM and SPH in modeling hypervelocity impact problems.* International Journal of Impact Engineering, 2009. **36**(2): p. 272-282.
27. Benson, D.J., *Computational methods in Lagrangian and Eulerian hydrocodes.* Computer Methods in Applied Mechanics and Engineering, 1992. **99**(2): p. 235-394.
28. Gingold, R.A. and J.J. Monaghan, *Smoothed particle hydrodynamics-theory and application to non-spherical stars.* Monthly Notices of the Royal Astronomical Society, 1977. **181**: p. 375-389.
29. Ryan, S., et al., *Characterizing the transient response of CFRP/Al HC spacecraft structures induced by space debris impact at hypervelocity.* International Journal of Impact Engineering, 2008. **35**(12): p. 1756-1763.
30. Clegg, R.A., et al., *Hypervelocity impact damage prediction in composites: Part I—material model and characterisation.* International Journal of Impact Engineering, 2006. **33**(1–12): p. 190-200.
31. Zhang, Q.M., et al., *SPH simulations of hypervelocity impact of al spheres on multi-plate structures.* International Journal of Modern Physics B, 2008. **22**(09n11): p. 1604-1611.
32. Liu, G.-R. and M. Liu, *Smoothed particle hydrodynamics: a meshfree particle method*. 2003, Singapore: World Scientific.
33. Anderson, J.D. and J. Wendt, *Computational fluid dynamics*. Vol. 206. 1995, Berlin: Springer.
34. Birdsall, C.K. and A.B. Langdon, *Plasma physics via computer simulation*. 2004, Boca Raton: CRC Press.
35. Ahrens, T., *Equation of state*, in *High-Pressure Shock Compression of Solids*. 1993, Springer. p. 75-113.
36. Libersky, L.D., et al., *High Strain Lagrangian Hydrodynamics: A Three-Dimensional SPH Code for Dynamic Material Response.* Journal of Computational Physics, 1993. **109**(1): p. 67-75.
37. Steinberg, D., S. Cochran, and M. Guinan, *A constitutive model for metals applicable at high-strain rate.* Journal of Applied Physics, 2008. **51**(3): p. 1498-1504.
38. Chuzel-Marmot, Y., R. Ortiz, and A. Combescure, *Three dimensional SPH–FEM gluing for simulation of fast impacts on concrete slabs.* Computers & Structures, 2011. **89**(23): p. 2484-2494.
39. De Vuyst, T., R. Vignjevic, and J.C. Campbell, *Coupling between meshless and finite element methods.* International Journal of Impact Engineering, 2005. **31**(8): p. 1054-1064.
40. Aerospace Specification Metals Inc.; Available from:

http://asm.matweb.com/search/SpecificMaterial.asp?bassnum=ma2024t4.

41. Liu, M., et al., *Modeling Hypervelocity-Impact-Induced Shock Waves for Characterizing Orbital Debris-Produced Damage.* Journal of Applied Mechanics, 2016. **83**(8): p. 081010.
42. Wang, C.H., J.T. Rose, and F.-K. Chang, *A synthetic time-reversal imaging method for structural health monitoring.* Smart Materials and Structures, 2004. **13**(2): p. 415-423.
43. Su, Z., L. Ye, and Y. Lu, *Guided Lamb waves for identification of damage in composite structures: A review.* Journal of sound and vibration, 2006. **295**(3): p. 753-780.
44. Qiu, L., et al., *A time reversal focusing based impact imaging method and its evaluation on complex composite structures.* Smart Materials and Structures, 2011. **20**(10): p. 105014.
45. Zhou, C., Z. Su, and L. Cheng, *Quantitative evaluation of orientation-specific damage using elastic waves and probability-based diagnostic imaging.* Mechanical Systems and Signal Processing, 2011. **25**(6): p. 2135-2156.
46. Su, Z., et al., *Assessment of delamination in composite beams using shear horizontal (SH) wave mode.* Composites Science and Technology, 2007. **67**(2): p. 244-251.